



# Development of dual-mode nitrite detection and multi-platform sensors based on magnetic COF-MOF hybrid nanocatalysts

Xinyi Wen<sup>a,b</sup>, Qingyuan Weng<sup>a</sup>, Ye Shao<sup>a</sup>, Zhizhen Yan<sup>a</sup>, Tianyi Sheng<sup>a</sup>, Yin Dai<sup>b,c,\*</sup>, Junli Hong<sup>a,b,\*\*</sup>

<sup>a</sup> The First Clinical Medical College, Nanjing Medical University, Nanjing, Jiangsu, 211166, China

<sup>b</sup> School of Pharmacy, Nanjing Medical University, Nanjing, Jiangsu, 211166, China

<sup>c</sup> Department of Pharmacy, The Second Affiliated Hospital of Nanjing Medical University, Nanjing, Jiangsu, 210011, China

## ARTICLE INFO

### Keywords:

Nanozyme

Nitrite

Dual-mode detection

Hydrogel platform

Cotton-based sensor

## ABSTRACT

Nitrite ( $\text{NO}_2^-$ ), a highly toxic contaminant, poses a severe threat to human health even at trace levels, necessitating rapid and precise detection methods. This study employed a dual-mode sensing strategy integrating covalent organic frameworks with  $\text{Fe}_3\text{O}_4/\text{Ce}$ -metal organic framework (MOF) nanozymes to construct peroxidase-mimetic hybrids. A Ce-MOF/TbBd catalyst (where Tb and Bd stand for the monomers) was used to oxidize 3,3',5,5'-tetramethylbenzidine (TMB) in the presence of  $\text{H}_2\text{O}_2$ , generating a blue product (oxTMB,  $\lambda_{\text{max}} = 651 \text{ nm}$ ). Subsequent diazotization with nitrite under acidic conditions yielded a yellow chromophore, enabling dual-wavelength colorimetric analysis via absorbance shifts at 445 nm (increase) and 651 nm (decrease). Three portable sensors—hydrogel, cotton fabric, and cotton swab platforms—were developed for on-site nitrite monitoring; they achieved detection limits of  $0.21 \mu\text{M}$  (colorimetric) and  $23.61 \mu\text{M}$  (RGB). The hydrogel sensor leverages ionic crosslinking for controlled chromogenic reactions, whereas cotton-based substrates utilize capillary action to enhance sensitivity and reduce matrix interference. This work not only advances multifunctional nanozyme design but also provides a practical toolkit for environmental and food safety applications, addressing critical challenges in real-time pollutant tracking with cost-effectiveness and operational simplicity.

## 1. Introduction

Nitrite is among the most common nitrogen-containing compounds in nature. Beyond the fields of industry and construction, it is widely employed in food processing (Karwowska and Kononiuk, 2022). It functions as a color additive, preservative agent, and antibacterial substance for meat products (McMahon et al., 2022; Michaud et al., 2009). However, excessive consumption of nitrite can pose numerous irreversible risks to the human body. Nitrite disrupts the body's oxygen transport system by converting normal oxygen-carrying hemoglobin into high levels of methemoglobin, leading to tissue hypoxia and even death (Liu et al., 2023; Gan et al., 2020). Additionally, nitrite reacts with amino acids to form nitrosamines, potent carcinogens that are associated with an increased risk of gastric and esophageal cancers, posing a significant threat to food safety and public health (Deveci and Tek, 2023; Schrenk et al., 2023). To address these concerns, the World Health Organization has set limits of nitrite in drinking water to  $3 \text{ mg/L}$  ( $65 \mu\text{M}$ ),

whereas the Joint Expert Committee on Food Additives recommends a maximum daily intake of  $0.06 \text{ mg/kg}$  ( $1.30 \mu\text{M}$ ). Therefore, developing highly sensitive, accurate, and user-friendly methods for nitrite detection in food and environmental samples is crucial for safeguarding health and promoting sustainable ecosystems and food supply chains.

The conventional analytical approaches widely used for nitrite detection are electrochemical analysis (Yi et al., 2021), gas chromatography (Zhang et al., 2024), surface-enhanced Raman scattering (Chen et al., 2016), and plasma atomic emission spectroscopy (Yang et al., 2025). Although effective, these techniques involve complex procedures and require sophisticated equipment and highly skilled operators. In contrast, optical biosensing approaches based on colorimetric and fluorescence readouts provide rapid, low-cost, and instrument-light alternatives. Colorimetric assays employ nanozyme or nanoparticle catalysts to drive chromogenic reactions that yield a visible color change within minutes; quantification is as simple as extracting RGB values via a smartphone camera or basic spectrophotometer (Ding et al., 2011;

\* Corresponding author. School of Pharmacy, Nanjing Medical University, Nanjing, Jiangsu, 211166, China.

\*\* Corresponding author. The First Clinical Medical College, Nanjing Medical University, Nanjing, Jiangsu, 211166, China.

E-mail addresses: [daiyin980607@163.com](mailto:daiyin980607@163.com) (Y. Dai), [junlihong@njmu.edu.cn](mailto:junlihong@njmu.edu.cn) (J. Hong).

<https://doi.org/10.1016/j.bios.2025.117825>

Received 22 May 2025; Received in revised form 23 July 2025; Accepted 25 July 2025

Available online 1 August 2025

0956-5663/© 2025 Elsevier B.V. All rights reserved, including those for text and data mining, AI training, and similar technologies.

Fernandes et al., 2020; Rao et al., 2021). Fluorescence sensors utilize environment-sensitive dyes or FRET pairs conjugated to bioreceptors; target binding triggers changes in emission intensity or wavelength, achieving ultra-low detection limits, real-time monitoring, and multiplexing capabilities (Rahmanian et al., 2024; Dadmehr et al., 2024a, 2024b). Additionally, its portability and cost-effectiveness render it ideal for extensive applications in food safety testing (Zhou et al., 2021; Zhao et al., 2024).

Covalent organic frameworks (COFs), which are porous crystalline materials, have shown considerable potential in numerous domains like catalysis (Marquez et al., 2019), separation (Mu et al., 2019), sensing (Guo et al., 2020), gas adsorption (Doonan et al., 2010), and energy storage (Zhu et al., 2025). Hybridization of metal-organic frameworks (MOFs) with COFs makes it feasible to combine the functional units of various metal ions and organic molecules, thus allowing for the customization of the performance of the composite materials (Li et al., 2020; Hou et al., 2023). The crystalline cellular structure of COFs not only serves as a protector, preventing the aggregation of MOFs and enhancing the overall stability, but also promotes transmission and exchange (Ahmad et al., 2025; Yang et al., 2022). Therefore, the construction of hierarchically porous crystalline MOF-COF nanocomposites represents a rational approach for enhancing the activity of mimetic enzymes.

In this study, a MOF-COF hybrid nanozyme was successfully fabricated by growing highly ordered porous crystals of TbBd (where Tb and Bd stand for the monomers) on the surface of a MOF ( $\text{Fe}_3\text{O}_4/\text{Ce-MOF}$ ). The nanozyme was developed such that the internal affinity for the organic precursor enables the successful adhesion of the TbBd network polyimide coating on the MOF (Banerjee et al., 2017; Xu et al., 2015). The COF unit was constructed from benzene-ring-containing condensed polymers. Its planar aromatic structure promotes the formation of coordination complexes with negatively charged  $\text{NO}_2^-$  ions through electrostatic interactions and  $\pi$ - $\pi$  stacking. According to density functional theory studies, the molecular orbitals of  $\text{NO}_2^-$  significantly overlap those of aromatic ligands, which effectively reduces the adsorption energy barrier and stabilizes the adsorbed state (Sharma et al., 2019; Adriaenssens et al., 2013). Moreover, the TbBd COF contains numerous C=N and -NH bonding sites that facilitate hydrogen bonding and dipole-ion interactions with  $\text{NO}_2^-$ , thereby enhancing the overall stability of the adsorption process (Karmakar et al., 2022). Furthermore, the magnetic property of  $\text{Fe}_3\text{O}_4$ , which serves as the core of the COF nanozyme, facilitates the recycling and reuse of the composite (Lu et al., 2007; Yan et al., 2018). The fabricated nanozyme not only possesses magnetic properties but also exhibits good dispersion, integrating the advantages of  $\text{Fe}_3\text{O}_4$ , MOFs, and COFs. Accordingly, a hydrogel-based detection platform with enhanced colorimetric sensitivity was developed, along with portable and user-friendly sensors devised on cotton fabric and cotton swab substrates. By leveraging the high adsorption capacity of cotton fabric and the abundant pore structure between fibers, the use of cotton swabs as carriers for nitrite detection enables efficient enrichment of target ions in the sample solution. The hydrophilic cellulose matrix demonstrates excellent compatibility with the chromogenic reagent, providing an optimal solid-phase reaction interface for accurate colorimetric analysis. Moreover, this material combines the advantages of low cost, ease of operation, and environmental friendliness, thereby satisfying the engineering requirements for sample pretreatment carriers in rapid detection technologies. The present work offers valuable perspectives on the design of MOF-COF hybrid nanozymes for nitrite detection and showcases the potential of employing colorimetric sensors for the rapid detection of environmental pollutants.

## 2. Experimental part

### 2.1. Reagents and instruments

Details of all the reagents and instruments used are provided in the

supplementary material.

### 2.2. Material synthesis

All reagents and detailed synthetic procedures used for preparing  $\text{Fe}_3\text{O}_4$  nanoparticles,  $\text{Fe}_3\text{O}_4/\text{Ce-MOF}$  core-shell particles, and the final  $\text{Fe}_3\text{O}_4/\text{Ce-MOF}/\text{TbBd}$  composite are provided in Section S1 of the supplementary material.

### 2.3. Peroxidase (POD)-like activity

To investigate the POD-like activity of the prepared COF, TMB was selected as the substrate. A mixture comprising 30  $\mu\text{L}$  of COF, 20  $\mu\text{L}$  of TMB at varying concentrations, 50  $\mu\text{L}$  of  $\text{H}_2\text{O}_2$ , and 100  $\mu\text{L}$  of acetate-sodium acetate buffer (pH = 4, 0.2 M) was incubated at 37  $^\circ\text{C}$  for 5 min. UV absorption spectra were recorded, and the Michaelis-Menten equation was used to calculate the Michaelis constant ( $K_m$ ) of the COF.

### 2.4. Dual-mode determination of nitrite

A volume of 10  $\mu\text{L}$  of nitrite solution with diverse concentrations was mixed with 10  $\mu\text{L}$  of TMB (10 mM), 50  $\mu\text{L}$  of  $\text{H}_2\text{O}_2$  (10 mM), 50  $\mu\text{L}$  of COF, and 380  $\mu\text{L}$  of acetate buffered saline (ABS solution) for dual-mode detection. The final reaction solution amounted to 500  $\mu\text{L}$ . After the reaction was conducted at 37  $^\circ\text{C}$  for 20 min, the UV absorption and RGB values of the resultant solution were determined. The limit of detection (LOD) was calculated according to the equation:  $\text{LOD} = 3\frac{\delta}{S}$ , where  $\delta$  is the standard deviation of the blank signal ( $n = 20$ ) and  $S$  is the slope of the calibration curve.

### 2.5. On-site sensor fabrication

Three platforms—hydrogel, cotton fabric, and cotton swab—were prepared by immobilizing  $\text{Fe}_3\text{O}_4/\text{Ce-MOF}/\text{TbBd}$  in a hydrogel, cotton fabric, or cotton swab, respectively. The protocols for sample application and color development, which required 20 min for the hydrogel and 5 min for the fabric and swab, are detailed in Section S2-S4 of the supplementary material.

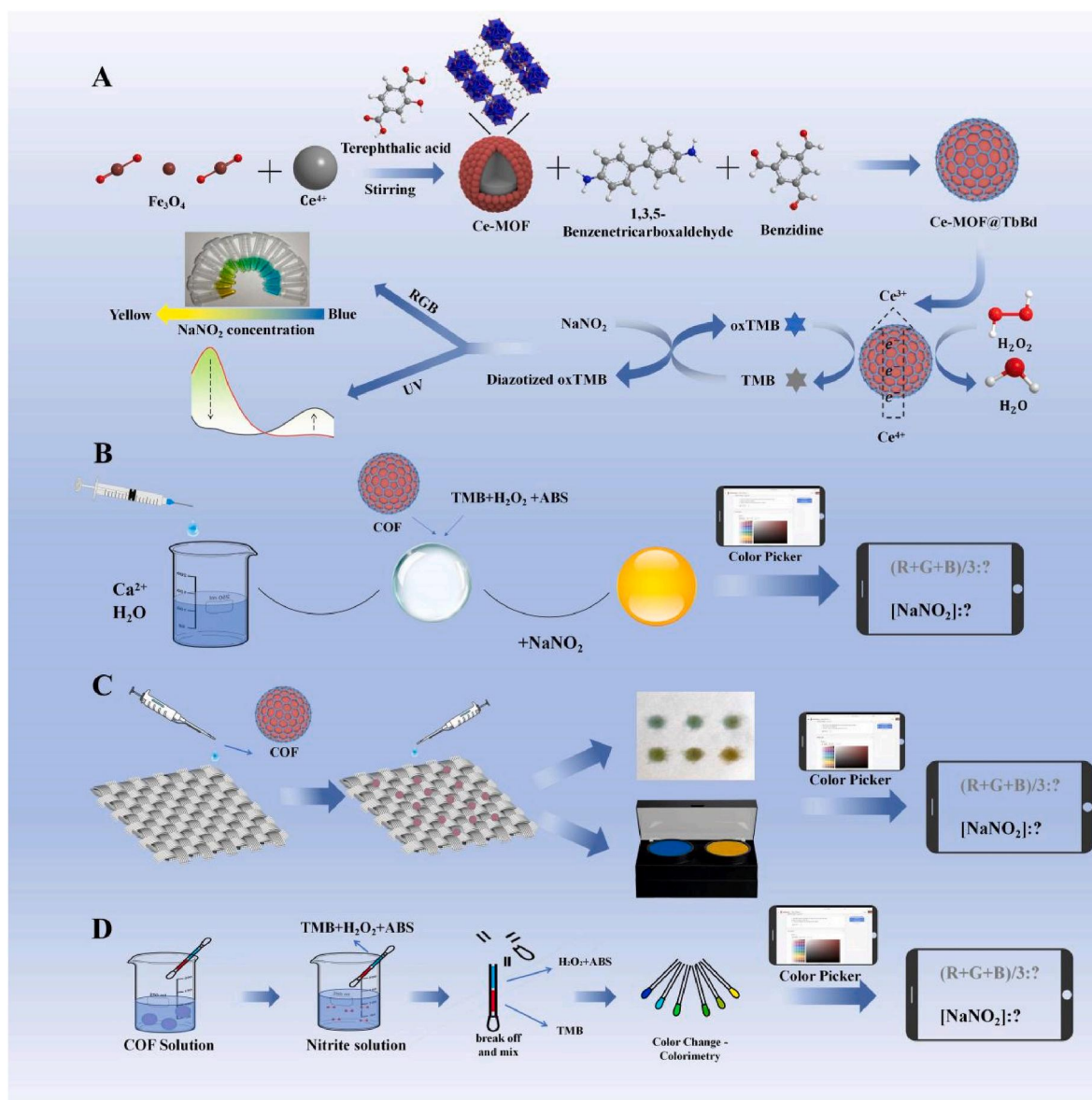
### 2.6. Analysis of actual samples

Healthy human serum, lake water, and fried chicken extract were chosen as samples after implementing certain pretreatment measures. The specifics are detailed in Section S5 of the supplementary material. These samples were utilized for dual-mode detection. The pH of the test samples was adjusted to 4 using an acetic acid/sodium acetate buffer, and dual-mode detection was carried out as described in Section 2.4.

## 3. Results and discussion

### 3.1. Feasibility and perceived strategies

The preparation of  $\text{Fe}_3\text{O}_4/\text{Ce-MOF}/\text{TbBd}$  is depicted in Scheme 1A. The COF demonstrated outstanding POD activity and stability, enabling dual-mode detection.  $\text{Fe}_3\text{O}_4/\text{Ce-MOF}/\text{TbBd}$  catalyzed  $\text{H}_2\text{O}_2$  to generate two hydroxyl radicals ( $\bullet\text{OH}$ ) that oxidized TMB to blue oxTMB. Consequently, the UV signal of oxTMB at 651 nm intensified in the presence of  $\text{H}_2\text{O}_2$  (Fig. 2A). Under acidic conditions, nitrite underwent diazotization with oxTMB to form a yellow diazo salt. Hence, the UV absorption of the detection system at 651 nm was attenuated, whereas the UV absorption at 445 nm was augmented (Fig. 2A). Thus, a dual-mode visualization colorimetric sensor for nitrite detection was implemented.



**Scheme 1.** (A) Nitrite detection mechanism based on  $\text{Fe}_3\text{O}_4/\text{Ce-MOF}/\text{TbBd}$ . (B) Nitrite detection platform combined with computer and hydrogel. (C) Nitrite detection platform combined with smartphone and cotton-fabric-based sensor. (D) Nitrite detection platform combined with smartphone and cotton swab sensor.

### 3.2. Characterization of $\text{Fe}_3\text{O}_4/\text{Ce-MOF}/\text{TbBd}$

Transmission electron microscopy (TEM; 120 kV; Fig. 1A) revealed a distinct “sandwich” architecture comprising an  $\text{Fe}_3\text{O}_4$  core, a conformal Ce-MOF shell, and an outer TbBd COF layer. Scanning electron microscopy (SEM; Fig. 1B) corroborated the presence of a continuous, interconnected porous network of the COF coating. Nitrogen adsorption-desorption measurements (BET; Fig. 1C) indicated a specific surface area of  $23.4 \text{ m}^2 \text{ g}^{-1}$  and an average pore diameter of 31 nm, which facilitated efficient substrate diffusion and adsorption. Vibrating sample magnetometry (VSM; Fig. 1D) yielded a saturation magnetization of  $45 \text{ emu g}^{-1}$ , confirming robust magnetic recoverability. X-ray diffraction (XRD; Fig. 1E) spectra exhibited distinct reflections attributable to  $\text{Fe}_3\text{O}_4$ , the Ce-MOF scaffold, and the TbBd COF, thereby verifying the successful integration of all components while preserving their crystallinity. The complete experimental parameters and the entire spectral dataset are presented in Section S5 of the supplementary material, as well as Fig. S1 and S3.

### 3.3. Structure-performance relationship analysis

TEM imaging, carried out at 120 kV (Fig. 1A), shows that the material has a uniform 100 nm  $\text{Fe}_3\text{O}_4$  core. This core is surrounded by a 20 nm thick Ce-MOF shell, and the outermost layer is covered with a 10 nm thick porous TbBd COF layer. This distinctive layered structure arrangement gives rise to two crucial characteristics: (i) a specific surface area of up to  $23.4 \text{ m}^2 \text{ g}^{-1}$ , and (ii) an average pore size of 31 nm (determined by the BET method; Fig. 1C). These features remarkably enhance the diffusion and adsorption capabilities of substrates such as TMB,  $\text{H}_2\text{O}_2$ , and  $\text{NO}_2^-$ . The VSM analysis results (Fig. 1D) verify a saturation magnetization of  $45 \text{ emu g}^{-1}$ , ensuring that the material can be easily recovered by magnetic force. Kinetic measurements further indicate that, compared with bare  $\text{Fe}_3\text{O}_4$ , the composite material reduces the Michaelis constant  $K_m$  for TMB from 0.42 mM to 0.30 mM (a 28 % decrease), while increasing the maximum reaction rate  $V_{max}$  by 35 %. The experimental results indirectly prove that the material we synthesized can enhance substrate affinity and catalytic efficiency.



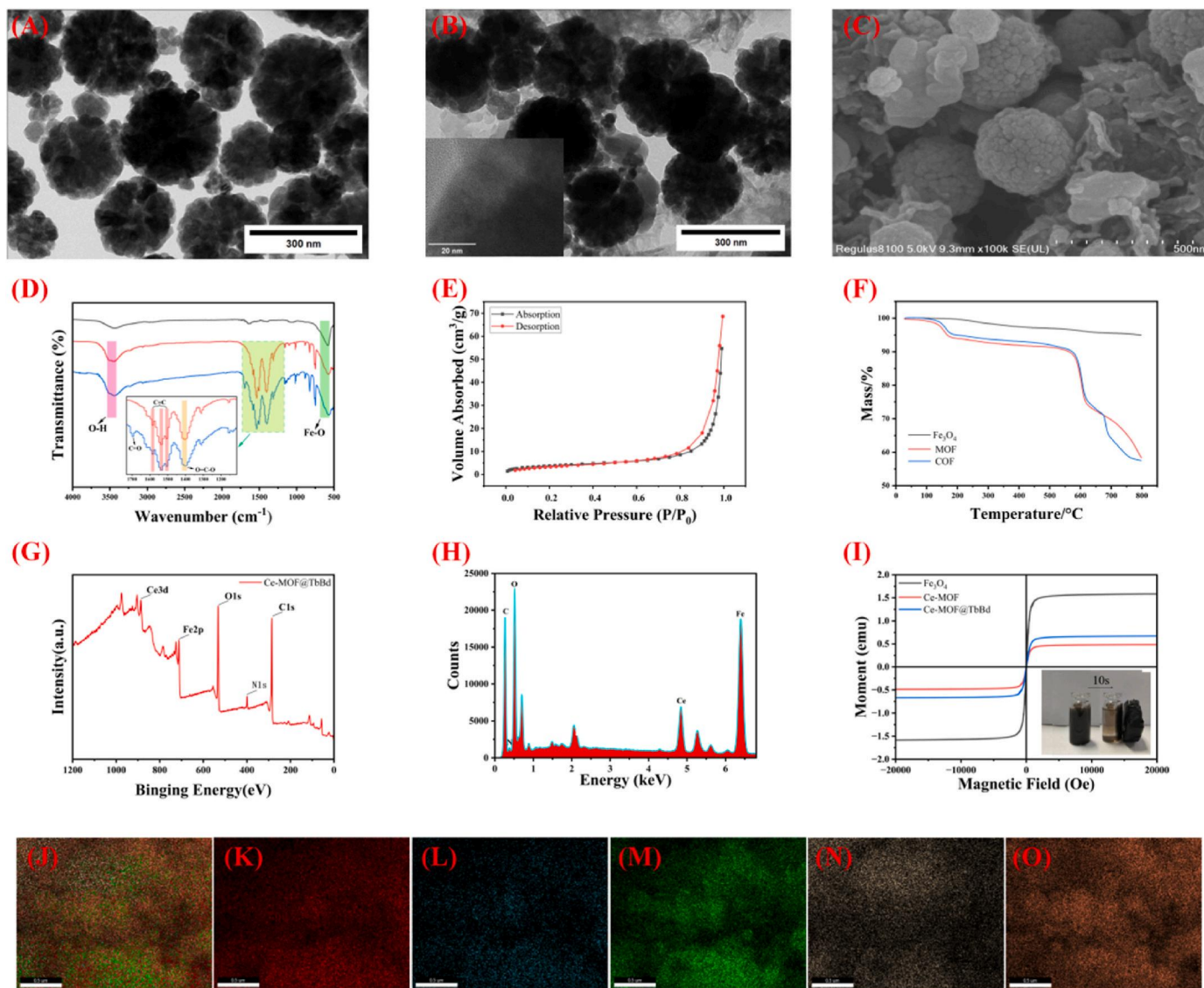


**Fig. 1.** (A) TEM images of  $\text{Fe}_3\text{O}_4/\text{Ce-MOF}$ . (B) TEM images of  $\text{Fe}_3\text{O}_4/\text{Ce-MOF/TbBd}$ . (C) SEM images of  $\text{Fe}_3\text{O}_4/\text{Ce-MOF/TbBd}$ . Inset of (B): HRTEM images of  $\text{Fe}_3\text{O}_4/\text{Ce-MOF/TbBd}$ . (D) FT-IR spectra of  $\text{Fe}_3\text{O}_4$ ,  $\text{Fe}_3\text{O}_4/\text{Ce-MOF}$ , and  $\text{Fe}_3\text{O}_4/\text{Ce-MOF/TbBd}$ . (E)  $\text{N}_2$  adsorption and desorption isotherms of  $\text{Fe}_3\text{O}_4/\text{Ce-MOF}$  and  $\text{Fe}_3\text{O}_4/\text{Ce-MOF/TbBd}$ . (F) TGA curves for  $\text{Fe}_3\text{O}_4$ ,  $\text{Fe}_3\text{O}_4/\text{Ce-MOF}$ , and  $\text{Fe}_3\text{O}_4/\text{Ce-MOF/TbBd}$ . (G) XPS spectrum of  $\text{Fe}_3\text{O}_4/\text{Ce-MOF/TbBd}$ . (H) EDS spectrum of  $\text{Fe}_3\text{O}_4/\text{Ce-MOF/TbBd}$ . (I) Hysteresis curves of  $\text{Fe}_3\text{O}_4$ ,  $\text{Fe}_3\text{O}_4/\text{Ce-MOF}$ , and  $\text{Fe}_3\text{O}_4/\text{Ce-MOF/TbBd}$ . (J)–(O): Elemental mapping of  $\text{Fe}_3\text{O}_4/\text{Ce-MOF/TbBd}$ .

### 3.4. POD-like activity of $\text{Fe}_3\text{O}_4/\text{Ce-MOF/TbBd}$

TMB was oxidized to oxTMB in the presence of  $\text{H}_2\text{O}_2$ , and oxTMB formed a diazonium salt with nitrite under acidic conditions, resulting in a color change from blue to green and then yellow (Fig. 2A). As shown in Fig. 2B, the hydroxyl radical ( $\bullet\text{OH}$ ) scavenger, isopropyl alcohol, decreased the absorbance at 651 nm ( $A_{651}$ ), indicating  $\bullet\text{OH}$  generation in the  $\text{Fe}_3\text{O}_4/\text{Ce-MOF/TbBd-H}_2\text{O}_2\text{-TMB}$  system. Fig. 2C shows that DMPO, used as a  $\bullet\text{OH}$  scavenger, produced the typical ESR characteristic peak (1:2:2:1) for  $\bullet\text{OH}$  radicals, confirming that  $\text{Fe}_3\text{O}_4/\text{Ce-MOF/TbBd}$  catalyzed  $\text{O}_2$  to generate  $\bullet\text{OH}$  (Cui et al., 2025). These findings demonstrate the POD-like activity of  $\text{Fe}_3\text{O}_4/\text{Ce-MOF/TbBd}$ .

The catalytic kinetics of  $\text{Fe}_3\text{O}_4/\text{Ce-MOF/TbBd}$  were analyzed using the Michaelis-Menten equation (Fig. 2D). The effects of various TbBd:MOF ratios on catalytic performance were also evaluated. When the TbBd dose was half the standard ratio, although  $K_m$  increased, the absorbance was too low for reliable results. At 1.5 times the standard ratio, COF aggregation increased, leading to blending issues and higher experimental error. The optimal TbBd:MOF ratio was determined to be

2:1.2:10, with a  $K_m$  of 0.31 mM.

The mechanism of peroxidase-like activity of the  $\text{Fe}_3\text{O}_4/\text{Ce-MOF/TbBd}$  composite material - including the contribution of active sites in different domains to the generation of  $\bullet\text{OH}$ , the Michaelis-Menten kinetic parameters, the multi-path interaction between  $\bullet\text{OH}$  and  $\text{NO}_2^-$ , and the reaction energy barrier profile based on DFT calculations is elaborated in detail in Section S6 and S7 of the supplementary material.

### 3.5. Impact of nitrite on $\text{Fe}_3\text{O}_4/\text{Ce-MOF/TbBd}$ -catalyzed POD-like reaction

As shown in Fig. S6A, the  $\text{Fe}_3\text{O}_4/\text{Ce-MOF/TbBd}$  and TMB system initially exhibited a blue color, as TMB was oxidized to oxTMB under the catalytic action of  $\text{Fe}_3\text{O}_4/\text{Ce-MOF/TbBd}$ . Upon the addition of 100  $\mu\text{M}$  nitrite, the solution color gradually transitioned to green. Concurrent nitrite addition led to a reduction in the UV-Vis absorption signal at 651 nm, whereas a new prominent peak appeared around 445 nm. Given that no significant interaction between nitrite and the nanocatalyst was observed (Fig. S4), this phenomenon can be attributed to the reaction

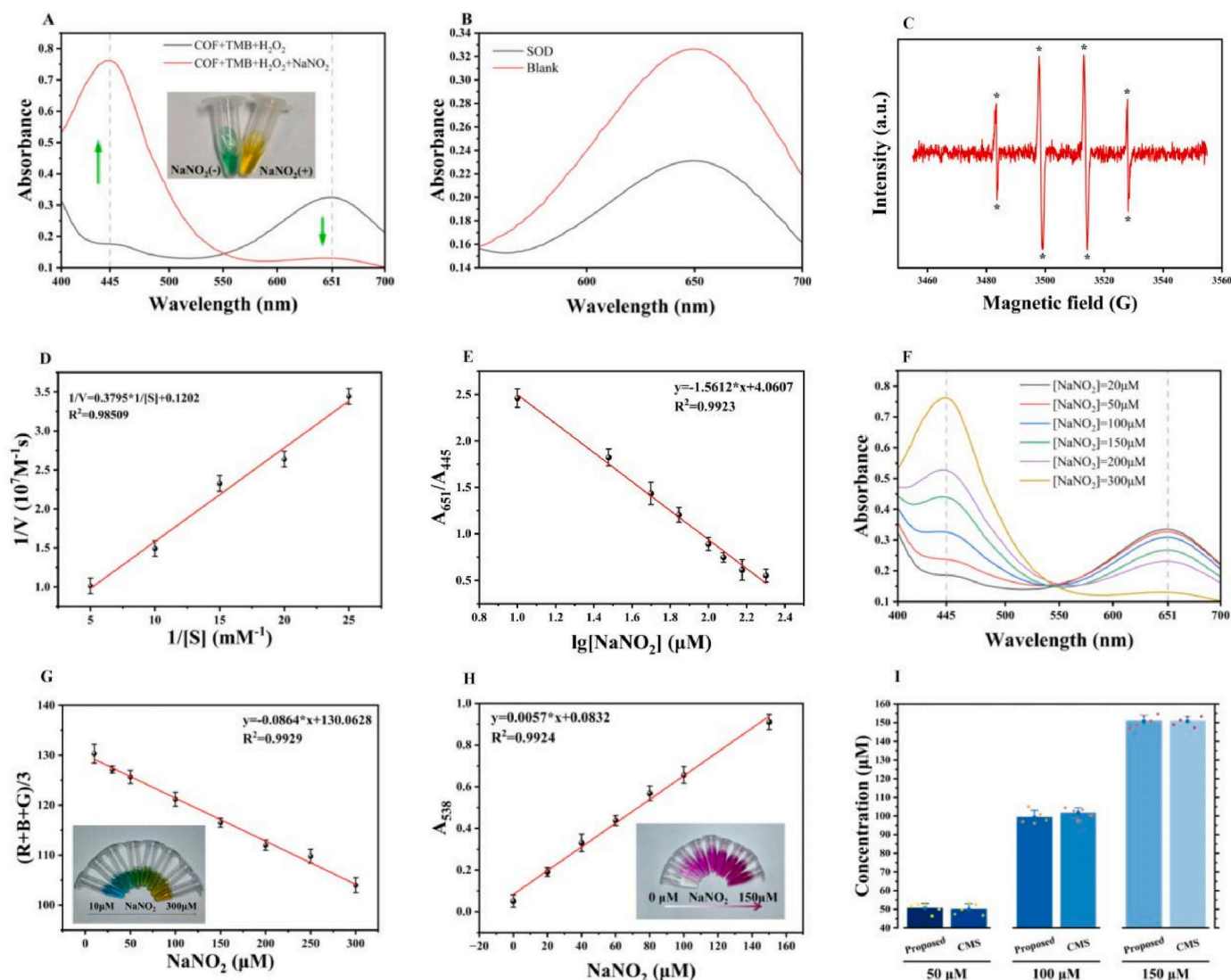


**Fig. 2.** (A) UV–Vis absorption spectra of different systems. (B) TMB + H<sub>2</sub>O<sub>2</sub>+Fe<sub>3</sub>O<sub>4</sub>/Ce-MOF/TbBd without or with a •OH radical scavenger (isopropyl alcohol). (C) Electron spin resonance (ESR) spectrum of DMPO + Fe<sub>3</sub>O<sub>4</sub>/Ce-MOF/TbBd. (D) Double-reciprocal plots of Fe<sub>3</sub>O<sub>4</sub>/Ce-MOF/TbBd ( $n = 3$ ). (E) Linearity of  $A_{651}/A_{445}$  versus the logarithm of nitrite concentration ( $n = 3$ ). (F) Changes in system UV absorption values at different nitrite concentrations. (G) Linear relationship between RGB value and nitrite concentration ( $n = 3$ ) and changes in system color at different nitrite concentrations. (H) Linearity of  $A_{538}$  versus nitrite concentration ( $n = 3$ ) and changes in system color at different nitrite concentrations. (I) Comparison of detection values for samples of different concentrations using two methods ( $n = 5$ ). (For interpretation of the references to color in this figure legend, the reader is referred to the Web version of this article.)

between oxTMB and nitrite. As illustrated in Fig. S6B, the aromatic primary amine group in oxTMB underwent a diazotization reaction with NO<sub>2</sub><sup>-</sup> in the acidic environment (pH = 4), resulting in a decrease in the original signal at 651 nm, and the emergence of a new signal at 445 nm, indicating the formation of diazotized oxTMB.

Control experiments were performed to further validate the occurrence of the diazotization reaction. As shown in Fig. S6C and S6D, under the catalytic influence of Fe<sub>3</sub>O<sub>4</sub>/Ce-MOF/TbBd, high concentrations of TMB were oxidized to blue oxTMB. Upon the addition of Ascorbic acid (AA), the blue oxTMB was reduced back to colorless TMB. In contrast, the addition of NO<sub>2</sub><sup>-</sup> resulted in a diazotization reaction with oxTMB, leading to the formation of green diazotized oxTMB, which could not be reduced back to colorless TMB by AA. These results further confirm the occurrence of a typical diazotization reaction between nitrite and oxTMB.

### 3.6. Dual-mode determination of nitrite

To ensure optimal experimental conditions, the reaction time,

temperature, and pH were evaluated. For both colorimetric (Fig. S1A and S1B) and RGB (Fig. S1D and S1E) modes, the ideal conditions were 20 min incubation at 37 °C. The pH of the reaction buffer significantly impacted enzyme activity, with optimal activity at pH 4 and 7 (Fig. S1C and S1F). Given the acidic conditions of the diazotization reaction, pH 4 was chosen as the optimal value.

Under these conditions, nitrite detection showed a linear decrease in the absorbance ratio ( $A_{651}/A_{445}$ ) with an increase in nitrite concentration (10–200 μM) ( $y = -1.5612x + 4.0607$ ,  $R^2 = 0.9923$ ), with an LOD of 0.21 μM, lower than that of most methods (Table S2), including the GB/T 5009.33–2016 method (LOD = 14.5 μM) (Fig. 2H). These results were validated through a *t*-test, which showed no significant difference between the methods (Table S3).

For portable applications, RGB values were extracted using Color-Picker software under controlled lighting (6500K, 80 % humidity). An adaptive RGB model helped address interference from color sample matrices. The (R + B + G)/3 ratio showed a strong linear correlation with nitrite concentration (10–300 μM) ( $y = -0.0864x + 130.0628$ ,  $R^2 = 0.9929$ ), with an LOD of 23.61 μM (Fig. 2G). The test results were

highly consistent when these two methods were applied to test the same sample at varying concentrations (Fig. 2I).

The data presented in Fig. 2E–G were derived from the same batch of samples. This approach guarantees consistency and continuity across diverse experimental conditions. The use of this common sample set underscores the interconnection of the presented data, strengthening the validity and coherence of the observed trends across these figures. Specific pairs of offset, high-chroma, and low-chroma effects are presented in the supplementary material.

### 3.7. On-site determination of nitrite based on hydrogel platform and cotton-fabric- and cotton-swab-based sensors

Aqueous nitrite solution was dripped onto the hydrogel sensor and allowed to react for 20 min. For portable biosensing, ColorPicker software was used to capture the colorimetric image, from which RGB chromaticity values were extracted. As shown in Scheme 1B, the RGB values correlated with nitrite concentration ( $y = -0.1594x + 106.322$ ,

$R^2 = 0.99509$ ), and the LOD was  $25.06 \mu\text{M}$  (Fig. 3A and B).

Different concentrations of  $\text{NaNO}_2$  ( $10 \mu\text{L}$ ) or samples were placed on the colorimetric interface of the cotton fabric for 5 min. Then,  $10 \mu\text{L}$  of a TMB ( $10 \text{ mM}$ ) and  $\text{H}_2\text{O}_2$  mixture in NaAc-HAc buffer ( $\text{pH } 4.0$ ) was added for the color reaction. After 5 min, the nitrite concentration was measured using the hydrogel method (Scheme 1C). The RGB value exhibited a linear correlation with nitrite concentration ( $y = -0.1829x + 131.3333$ ,  $R^2 = 0.9911$ ), and the LOD was  $23.12 \mu\text{M}$  (Fig. 3C and D). This cotton-based sensor leverages the capillary action of the fabric for synchronous sample transportation and reaction, offering a low-cost, scalable, and efficient solution for rapid on-site detection.

Different sample concentrations ( $500 \mu\text{L}$ ) were applied to the pre-functionalized swab tip and incubated for 1 min. The hierarchical porous structure of the cotton fibers enabled rapid permeation and molecular enrichment. The swab handle was then manually broken, and atmospheric pressure and gravity drove the flow of  $\text{H}_2\text{O}_2$  and TMB solutions from the swab body to the tip, ensuring self-mixing of reagents (Scheme 1D). After a 2 min chromogenic reaction, the color change at

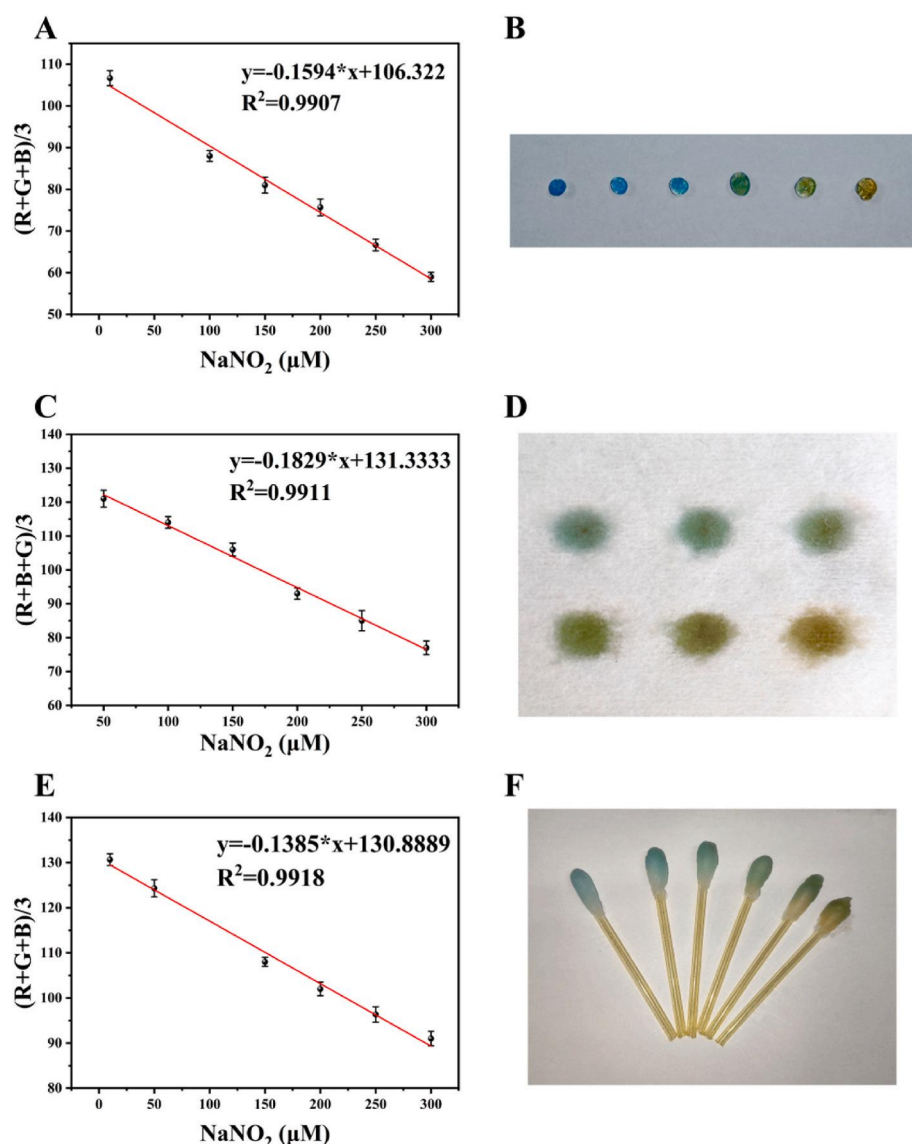


**Fig. 3.** (A) Linear relationship between RGB value and nitrite level in hydrogel platform ( $n = 3$ ). (B) Changes in color of hydrogel platform system at different nitrite concentrations. (C) Linear relationship between RGB value and nitrite level in cotton-fabric-based sensor system at different nitrite concentrations. (D) Changes in color of cotton-fabric-based sensor system at different nitrite concentrations. (E) Linear relationship between RGB value and nitrite level in cotton-swab-based sensor ( $n = 3$ ). (F) Changes in color of cotton swab sensor system at different nitrite concentrations. (For interpretation of the references to color in this figure legend, the reader is referred to the Web version of this article.)



the swab apex was captured using a smartphone imaging system (Fig. 3F), and analyte concentrations were quantified using ColorPicker software. The results showed a strong linear correlation ( $y = -0.1385x + 130.8889$ ,  $R^2 = 0.9918$ ) between colorimetric intensity and analyte concentration (10–300  $\mu\text{M}$ ), with an LOD of 29.49  $\mu\text{M}$  (Fig. 3E). This sensor utilizes the cotton swab's fibrous network for spatial decoupling of sample pretreatment and signal visualization, offering a practical, on-site detection solution.

### 3.8. Comprehensive performance evaluation of system/technology

To evaluate the selectivity of the dual-mode sensor for nitrite, we tested its response to common compounds in polluted environments, including  $\text{CuSO}_4$ ,  $\text{PbCl}_2$ ,  $\text{CaCl}_2$ ,  $\text{NaCO}_3$ ,  $\text{NaCl}$ ,  $\text{K}_2\text{CO}_3$ ,  $\text{ZnSO}_4$ , and  $\text{MgSO}_4$ . Even at ten times the concentration of nitrite (10  $\mu\text{M}$ ), these substances caused negligible interference with fluorescence or colorimetric quantification (Fig. 4A). Stored at 4  $^\circ\text{C}$  for 120 days,  $\text{Fe}_3\text{O}_4/\text{Ce-MOF}/\text{TbBd}$  showed minimal changes in both POD-like and RGB activities, confirming its stability. Further long-term and harsh condition studies are planned (Fig. 4B).

Following GB/T 5009.33–2016, the sensor's detection metrics for nitrite, including relative error, precision, and repeatability (RSD), were analyzed. Eight replicate measurements of 10  $\mu\text{M}$  nitrite resulted in RSD values under 2.5 % for fluorescence and 3.0 % for colorimetric modes, indicating excellent repeatability (Fig. 4C).

For specificity, a mixed interference system (10  $\mu\text{M}$  of all eight potential interferents) was tested. The sensor's response to nitrite in this system showed less than 4 % deviation from the pure nitrite case, confirming its high specificity (Fig. 4D). These results demonstrate the sensor's robustness for reliable nitrite quantification in complex environments.

We conducted a comprehensive evaluation of the system's practical application performance by measuring the duration from sample to result. This process typically takes an average of  $20 \pm 2$  min, covering the entire sequence from sample input to signal acquisition. This effectively reflects the system's efficiency and convenience. Table S6 summarizes this crucial metric and emphasizes the system's response time advantage over recent state-of-the-art approaches. Through the optimization of catalytic kinetics and the simplification of the lifting operation process, the system's response speed has been increased by over

30 %. Fig. S4 depicts the time required for the cotton swab-based sensor to detect nitrite. These efficient enhancements demonstrate that the system performs admirably in rapid response and detection, particularly in fields where speed, promptness, and directness are highly valued, such as environmental monitoring and food safety testing.

### 3.9. Determination of nitrite in human serum, fried chicken extract, and lake water

To evaluate the practicality of the sensor for real sample detection, nitrite at varying concentrations was added to human whole blood, fried chicken extract, and lake water, and the recovery rates were measured. In colorimetric mode, the recovery rates ranged from 97.78 % to 104.64 %, 97.84 %–102.94 %, and 95.04 %–101.98 %, respectively. In RGB mode, the corresponding recovery ranges were 99.74–105.72 % (Table 1), 97.25–103.78 % (Table S4), and 96.35–101.92 % (Table S5). These results demonstrate that the dual-mode sensor is effective for nitrite detection in real samples, showing high reliability and practicality. Notably, the colorimetric and RGB results align, confirming the accuracy of both modes.

The dual-mode strategy offers several advantages over single-mode detection, including complementarity, versatility, and multi-signal read-out, making it more reliable and applicable. This approach can be further developed into a rapid nitrite detection kit with key benefits: (1) the MOF-COF complex structure and nanozyme significantly enhance sensitivity; (2) the magnetic core facilitates efficient enzyme recovery, addressing the limitation of single-use detection and reducing chemical pollution; (3) the cotton-fiber-based interface enriches target substances through capillary action, enabling a streamlined “sampling-enrichment-detection” process within 5 min, eliminating the need for complex sample preparation.

This design integrates the high catalytic activity of nanozymes with on-site detection practicality, offering chromatography-level sensitivity and operational simplicity. It provides a cost-effective and efficient solution for food safety monitoring and early pollutant warning systems.

## 4. Conclusion

In summary, this study represents a comprehensive and innovative approach for dual-mode nitrite detection through the integration of

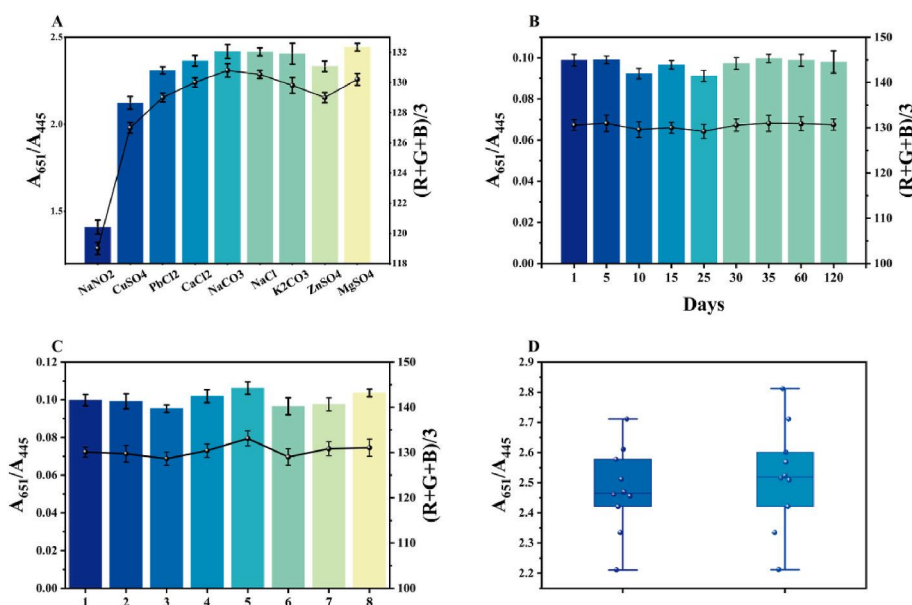


**Fig. 4.** (A) Nitrite selectivity of reaction system ( $n = 3$ ). (B) Stability of dual-mode sensor based on  $\text{Fe}_3\text{O}_4/\text{Ce-MOF}/\text{TbBd}$  over 120 days ( $n = 3$ ). (C) Precision of dual-mode sensor based on  $\text{Fe}_3\text{O}_4/\text{Ce-MOF}/\text{TbBd}$  ( $n = 3$ ). (D) Specificity of dual-mode sensor based on  $\text{Fe}_3\text{O}_4/\text{Ce-MOF}/\text{TbBd}$  ( $n = 10$ ).

**Table 1**  
Determination results of nitrite in healthy human serum ( $n = 3$ ).

Sample	Detected ( $\mu\text{M}$ )	Added ( $\mu\text{M}$ )	Colorimetric sensor			RGB sensor		
			Founded ( $\mu\text{M}$ )	Recovery (%)	RSD (%)	Founded ( $\mu\text{M}$ )	Recovery (%)	RSD (%)
1	ND	5	4.974	99.48	0.29	4.987	99.74	6.21
		10	10.464	104.64	0.12	10.532	105.32	5.68
		15	15.592	103.95	0.06	15.238	101.59	3.63
2		5	4.889	97.78	0.90	5.024	100.48	2.16
		10	10.325	103.25	0.13	10.572	105.72	2.56
		15	15.485	103.23	0.94	15.232	101.55	3.77
3		5	4.911	98.22	0.40	5.112	102.24	2.10
		10	10.166	101.66	0.16	10.306	103.06	3.43
		15	15.295	101.97	0.68	14.983	99.89	4.65

ND = Not detected.

advanced nanozyme technology with versatile sensing platforms. The hydrogel-based sensor demonstrates enhanced colorimetric sensitivity and operational stability, leveraging ionic crosslinking to achieve controlled chromogenic reactions for precise on-site quantification. The cotton-fabric-based sensor capitalizes on the inherent capillary action and high adsorption capacity of cellulose substrates, enabling efficient sample enrichment and synchronous signal readout with minimal matrix interference. Furthermore, the cotton-swab-based sensor exploits the three-dimensional porous architecture of medical-grade absorbent cotton, facilitating rapid analyte permeation, molecular enrichment, and reagent self-mixing via axial flow control attributes that are indispensable for field-deployable diagnostics. Collectively, these platforms synergize the excellent catalytic ability of  $\text{Fe}_3\text{O}_4/\text{Ce-MOF}/\text{TbBd}$  nanozymes with the practicality of low-cost user-friendly substrates, addressing critical challenges in environmental monitoring and food safety. Their robust performance in complex matrices, coupled with dual-mode verification capabilities, underscores their potential as reliable tools for mitigating nitrite-related hazards in real-world scenarios. This work not only advances the design of multifunctional nanozymes but also establishes a paradigm for developing portable, eco-friendly detection systems tailored to safeguard public health and ecological integrity.

5. Environmental implications

This work delivers a practical, eco-friendly approach to nitrite surveillance that can significantly mitigate environmental and public-health risks. By coupling a recyclable magnetic nanozyme with simple low-cost substrates (hydrogel beads and cotton fabrics and swabs), it enables rapid, on-site screening of water and food without reliance on centralized laboratories. Minimal reagent use and efficient magnetic recovery dramatically reduce chemical waste and secondary pollution, while the portability of the sensors supports decentralized, frequent monitoring in remote or resource-limited settings. Together, these features pave the way for broader cost-effective deployment of nitrite testing to improve early warning of contamination events and safeguard ecosystems and human health.

CRediT authorship contribution statement

**Xinyi Wen:** Writing – review & editing, Writing – original draft, Visualization, Validation, Supervision, Project administration, Methodology, Investigation, Funding acquisition, Data curation, Conceptualization. **Qingyuan Weng:** Writing – original draft, Visualization, Validation, Software, Resources, Methodology, Formal analysis, Data curation. **Ye Shao:** Investigation, Formal analysis, Data curation, Conceptualization. **Zhizhen Yan:** Methodology, Investigation, Funding acquisition, Data curation. **Tianyi Sheng:** Formal analysis, Data curation, Conceptualization. **Yin Dai:** Writing – review & editing, Writing – original draft, Visualization, Validation, Software, Project administration, Methodology, Investigation, Formal analysis, Data curation,

Conceptualization. **Junli Hong:** Writing – review & editing, Writing – original draft, Methodology, Investigation, Funding acquisition, Formal analysis, Data curation, Conceptualization.

Declaration of competing interest

The authors declare that they have no known competing financial interests or personal relationships that could have appeared to influence the work reported in this paper.

Acknowledgment

This research was funded by the Nanjing Medical University Undergraduate Innovation and Entrepreneurship Training Program Project (202410312057Z), Science and Technology Development Fund of Nanjing Medical University (NMUB20240003), Medical Research Foundation of Jiangsu Commission of Health (No. Z2020009), National Natural Science Foundation of China (81202853) and China Postdoctoral Science Foundation (No. 2017M621789).

Appendix A. Supplementary data

Supplementary data to this article can be found online at <https://doi.org/10.1016/j.bios.2025.117825>.

Data availability

The authors do not have permission to share data.

References

Adriaenssens, L., Estarellas, C., Vargas Jentzsch, A., Martinez Belmonte, M., Matile, S., Ballester, P., 2013. *J. Am. Chem. Soc.* 135 (22), 8324–8330.  
Ahmad, K., Awan, M.M.A., Kashif, M., Qureshi, K., Ahmad, I., Nazir, M.A., Shah, H.U.R., Ashfaq, M., 2025. *Hybrid Adv.* 9, 100419.  
Banerjee, T., Haase, F., Savasci, G., Gottschling, K., Ochsenfeld, C., Lotsch, B.V., 2017. *J. Am. Chem. Soc.* 139 (45), 6228–16234.  
Chen, J., Pang, S., He, L., Nugen, S.R., 2016. *Biosens. Bioelectron.* 85, 726–733.  
Cui, Y., Zhao, N., Wang, S., Yan, H., Han, D., 2025. *Biosens. Bioelectron.* 287, 117726.  
Dadmehr, M., Korouzhdehi, B., Hosseini, M., 2024a. *Microchem. J.* 205, 111127.  
Dadmehr, M., Sangachin, E.A., Bazzi, F., Li, J., Hosseini, M., 2024b. *TrAC, Trends Anal. Chem.* 178, 117836.  
Deveci, G., Tek, N.A., 2023. *J. Sci. Food Agric.* 104 (5), 2551–2560.  
Ding, S., Gao, J., Wang, Q., Zhang, Y., Song, W., Su, C., Wang, W., 2011. *J. Am. Chem. Soc.* 133 (49), 19816–19822.  
Doonan, C.J., Tranchemontagne, D.J., Yaghi, O.M., 2010. *Nat. Chem.* 2 (10), 235–238.  
Fernandes, G.M., Silva, W.R., Barreto, D.N., Lamarca, R.S., Lima Gomes, P.C.F., Flávio da S Petruc, J., Batista, A.D., 2020. *Anal. Chim. Acta* 1135, 187–203.  
Gan, L., Su, Q., Chen, Z., Yang, X., 2020. *Appl. Surf. Sci.* 530, 147269.  
Guo, L., Song, Y., Cai, K., Wang, L., 2020. *Spectrochim. Acta. A. Mol. Biomol. Spectrosc.* 227, 117703.  
Hou, C., Cheng, D., Zou, S., Gao, J., Wang, J., Wang, Y., 2023. *J. Environ. Chem. Eng.* 11 (5), 110914.  
Karmakar, A., Velasco, E., Li, J., 2022. *Natl. Sci. Rev.* 9 (7), nwac091.  
Karwowska, M., Kononiuk, A., 2022. *Food Chem. Toxicol.* 165, 113105.  
Li, F., Cui, W., Jiang, W., Zhang, C., Liang, R., Qiu, J., 2020. *J. Hazard. Mater.* 392, 122333.



- Liu, J., Gong, L., Chen, H., Gui, J., Zhu, X., Liu, M., Zhang, Y., Yao, S., 2023. *ACS Appl. Nano Mater.* 6 (7), 5879–5888.
- Lu, A., Salabas, E.L., Schüth, F., 2007. *Angew. Chem. Int. Ed.* 46 (8), 1222–1244.
- Marquez, S., Liu, J., Morales-Narváez, E., 2019. *Curr. Opin. Environ. Sci. Health.* 10, 1–8.
- McMahon, N.F., Brooker, P.G., Pavey, T.G., Leveritt, M.D., 2022. *Crit. Rev. Food Sci. Nutr.* 64 (9), 2673–2694.
- Michaud, D.S., Holick, C.N., Batchelor, T.T., Giovannucci, E., Hunter, D.J., 2009. *Am. J. Clin. Nutr.* 90 (3), 570–577.
- Mu, X., Zhan, J., Wang, J., Cai, W., Yuan, B., Song, L., Hu, Y., 2019. *J. Colloid Interface Sci.* 539, 609–618.
- Rahmanian, H., Malekkiani, M., Dadmehr, M., Es'haghi, Z., Moshirian-Farahi, S.S., 2024. *Anal. Chim. Acta* 1323, 343085.
- Rao, H., Xue, X., Luo, M., Liu, H., Xue, Z., 2021. *Chin. Chem. Lett.* 32 (1), 25–32.
- Schrenk, D., Bignami, M., Bodin, L., Chipman, J.K., del Mazo, J., Hogstrand, C., Hoogenboom, L. (Ron), Leblanc, J., Nebbia, C.S., Nielsen, E., Ntzani, E., Petersen, A., Sand, S., Schwerdtle, T., Vleminckx, C., Wallace, H., Romualdo, B., Fortes, C., et al., 2023. *EFSA J.* 21 (3), e07884.
- Sharma, A., Kim, D., Park, J., Rakshit, S., Seong, J., Jeong, G.H., Kwon, O., Lah, M.S., 2019. *Commun. Chem.* 2 (1), 13.
- Xu, H., Gao, J., Jiang, D., 2015. *Nature Chem.* 7 (11), 905–908.
- Yan, Y., Lu, Y., Wang, B., Gao, Y., Zhao, L., Liang, H., Wu, D., 2018. *ACS Appl. Mater. Interfaces* 10 (31), 26539–26545.
- Yang, L., Wang, Y., Yuan, J., Wang, G., Cao, Q., Fei, H., Li, M., Shao, J., Li, H., Lu, J., 2022. *Chem. Eng. J.* 446, 137095.
- Yang, R., Yang, L., Yang, J., Li, Z., Zheng, C., 2025. *Talanta* 291, 127836.
- Yi, W., Li, Z., Dong, W., Han, C., Guo, Y., Liu, M., Dong, C., 2021. *ACS Appl. Nano Mater.* 5 (1), 216–226.
- Zhang, Z., Zhang, T., Yang, D., Yang, Y., Zhao, X., Fan, Y., Zhang, J., Yang, J., 2024. *J. Environ. Chem. Eng.* 12 (2), 112218.
- Zhao, X., Lu, Y., Wu, J., Yang, Y., Li, B., Li, H., Sun, Y., Yan, X., Liu, X., Lu, G., 2024. *Biosens. Bioelectron.* 263, 116622.
- Zhou, Y., Huang, X., Hu, X., Tong, W., Leng, Y., Xiong, Y., 2021. *Biosens. Bioelectron.* 190, 113386.
- Zhu, L., Cao, Y., Xu, T., Yang, H., Wang, L., Dai, L., Pan, F., Chen, C., Si, C., 2025. *Energy Environ. Sci.* 18 (12), 5675–5739.